The effects of Fe and Al on the phase transformations and mechanical behavior of β-Ti alloy Ti-11at.%Cr

Authors: J. Ballor [a*], A. A. Shawon [a], A. Zevalkink [a], T. Sunaoshi [b], S. Misture [c], C.J. Boehlert [a]

[a] Department of Chemical Engineering and Material Science, Michigan State University, East Lansing, Michigan, United States

[b] Hitachi High-Tech America, Inc., Clarksburg, Maryland, United States

[c] Inamori School of Engineering, Alfred University, Alfred, New York, United States

[*]corresponding author: ballorj2@msu.edu

Abstract

Alloy composition is important for developing desired microstructures in beta-titanium (β-Ti) alloys during thermomechanical processing. In this work, the relatively low-cost alloying elements iron (Fe) and aluminum (Al) were added to a base Ti-11at%chromium (Cr) alloy and in-situ and ex-situ examination of the microstructural evolution and mechanical properties during tension, hardness, elevated temperature X-ray diffraction (XRD) and resonance ultrasound spectroscopy (RUS) were performed. The 400 °C XRD revealed that Ti-11at%Cr underwent β-to-ω and β-to-α transformations. Adding 0.85at% Fe reduced the volume fraction of the ω- and α-phases, and adding 5.3at% Al inhibited the β-to-ω transformation. The 400 °C RUS showed that the alloys containing the ω phase exhibited an increase in shear modulus (G) of ~140%, while the ω-free alloys exhibited an increase of only ~102%. The hardness and strength values of the ω-containing Ti-11Cr and Ti-11Cr-0.85Fe increased with increased ω-phase volume fraction when the ω/α ratio was greater than 0.25. The relationship between ω/α volume ratios and mechanical properties is discussed.

Keywords

Titanium alloys, phase transformation, hardness, stress/strain measurements, X-ray analysis, electron microscopy

Introduction

β-titanium (β-Ti) alloys exhibit relatively high strength-to-weight ratios compared to other structural metals, and their mechanical properties can be tuned by transforming the metastable body-centered-cubic (BCC) β phase into other metastable and stable phases [1]. However, their relatively high cost limits their widespread use in industries where steels or aluminum alloys can meet the property requirements at a fraction of the cost. The type and content of alloying elements influences the cost of β-Ti alloys, which are commonly alloyed with relatively expensive elements such as vanadium and molybdenum. Before implementing less costly alloying elements, such as chromium, aluminum, and iron, into industrially used β-Ti alloys, a systematic understanding of how alloy composition and processing affects the microstructure and mechanical properties is necessary.

Alloy composition can significantly impact the phase transformations in β-Ti alloys. The relative stability of the β phase affects which phase transformations occur during processing, and a threshold content of elements that increase the β-phase stability (known as β stabilizers) is needed to retain the metastable β phase at room temperature (RT) [1]. In contrast, alloying elements that stabilize the α phase (known as α-stabilizers, promote α-phase formation during processing. Al is a common α-stabilizer that promotes

increased strength and hardness of β-Ti alloys. Certain alloying elements can promote the formation of the metastable ω phase, and aging between 300 °C and 400 °C is commonly used to induce the β-to-ω transformation [2].

The ω phase is known to increase hardness and strength, but it is also tends to decrease the elongation-to-failure [2]. Brittle failure is common when the ω phase is present. The ω-assisted α phase forms at the nanoscale [3], and fine-grained α-phase microstructures have exhibited high hardness and strength without experiencing brittle failure [4–7].

In this work, the evolution of the β-, α-, and ω-phase during 400 °C aging was explored in the titanium-chromium (Ti-Cr) alloy system, where both β-to-ω and β-to-α phase transformations occur [8–10]. Ti-11Cr(at.%) was considered the baseline alloy, which was modified using 0.85at.% of the β-phase stabilizer iron (Fe) and/or 5.3at.% aluminum (Al), and the effect of aging on the microstructure and mechanical properties (hardness, Young's modulus, tensile strength and elongation-to-failure were evaluated. In-situ X-ray diffraction (HTXRD) and resonance ultrasound spectroscopy (RUS) were performed to investigate the phase transformations and shear modulus, respectively, during 400 °C aging. Fe and Al significantly affected the phase transformations and mechanical properties of the Ti-Cr alloy system.

Materials and Methods

Ti-11Cr(at.%) (TC), Ti-11Cr-0.85Fe(at.%) (TCF), Ti-11Cr-5.3Al(at.%) (TCA), and Ti-11Cr-0.85Fe-5.3Al(at.%) (TCFA) were levitation melted in a 2 kg, 90Dx80L LEV levitation induction furnace and hot forged at approximately 1047 °C into 25 x 60 x 250 mm^3 blocks. The alloys were homogenized during a 900 °C anneal for 1 h in vacuum, followed by ice-water quenching at an estimated cooling rate of 34.7 $°Cs^{-1}$. These processing steps were performed at Daido Steel Company, Ltd. (Nagoya, Japan), and the measured compositions of the alloys were reported previously [11].

Samples for tensile testing were electrodischarge machine (EDM) cut from the forged blocks into a "dogbone-shaped" geometry with a gage length of 30 mm, gage width of 3.5 mm, and overall sample thickness of 1.1 mm. To induce the β-to-ω and/or β-to-α transformations, these samples were heated at a rate of 15 $°Cmin^{-1}$ to 400 °C in a quartz vacuum tube furnace for either 0.75, 1.5, 3, 6, or 12 hours, followed by air-quenching to RT. A thermocouple was used to monitor the sample temperature throughout the heat treatment. Before tensile testing the sample surfaces were polished using 320 grit silicon carbide (SiC) paper and water to remove any oxides and surface defects.

Samples for Vickers microhardness and scanning electron microscopy (SEM) imaging were cut from the grip sections of the aged samples. Hardness testing samples were polished to a mirror finish, and 10 tests were performed per sample according to ASTM Standard E92-17 using a 500 gf load and a dwell time of 15 s. After polishing, the SEM samples were ion milled using a Hitachi IM4000Plus at 6 kV to reveal the microstructure. SEM photomicrographs of 70x, 10kx, and 80kx magnifications were taken using a Hitachi Regulus 8230 SEM, which contained a photodiode backscattered electron (BSE) detector, operated at a 5 kV accelerating voltage. ImageJ software was used with the BSE SEM photomicrographs to estimate the volume fractions of the precipitates. Subsets of each image were isolated and a threshold saturation value was set. Pixels that were darker than a set threshold value were counted to determine the volume fraction of the precipitates.

XRD samples were polished using 320 grit SiC paper and water to remove any macroscopic surface defects or oxidation-affected surface layers. The final sample dimensions were 17 x 17 x 1.1 mm. RT XRD was performed on a Bruker D8 Advance with an automatic sample changer. Cu-Kα X-ray radiation was used and data was collected over a 2θ range of 25° to 75°. 400 °C XRD was performed using a Bruker-AXS

(Madison, WI) D8 diffractometer with an automatic sample changer, a Vantec linear position-sensitive detector, Cu-Kα radiation, and an Anton-Paar HTK1200 furnace with ultra-high-purity nitrogen gas to prevent oxidation during heating. The heating rate was 30 °Cmin^{-1} except for the beginning and ending of the heating process, which had an exponential and logarithmic character, respectively. Data was collected in situ over a 2θ range of 25° to 75° every 0.5 h during the 12 h 400 °C exposure. Along with analyzing the XRD scans for peaks associated with Ti oxides, samples were visually inspected after the HTXRD tests to determine if oxidation occurred during testing. No evidence of oxidation was found in the data or during the visual inspection.

For each alloy, Rietveld analysis was performed on the 400 °C XRD data to determine the volume fractions and lattice parameters of the β, α, and ω phases at each 0.5 h time step. The Rietveld refinement and lattice parameter calculations were performed using the Topas software package (Bruker-AXS). The Rietveld lattice parameter refinement for TC was accomplished using software suite PDXL version 2 [12], and the weighted-profile residual for each Rietveld analysis was between 4.9% and 7.9%. Table 1 contains the crystallographic information of the phases considered for the Rietveld refinement as cited in the ICSD database.

Table 1. The crystallographic data of the β, α, and ω phases used for the Rietveld refinement.

Phase	a (Å)	b (Å)	c (Å)	Structure	Space Group	Atomic Positions (x,y,z)	Reference
β	3.21	-	-	Cubic	$Im\bar{3}m(229)$	(0,0,0) (1/2,1/2,1/2)	[13]
α	2.95	-	4.69	Hexagonal	$P6_3/mmc(194)$	(0,0,0) (1/3,2/3,1/2)	[14]
ω	4.60	-	2.82	Hexagonal	P6/mmm(191)	(0,0,0) (1/3,2/3,1/2) (2/3,1/3,1/2)	[15]

Samples for the RUS measurements were EDM cut from the forged blocks into cubes with dimensions of 4.5 x 5 x 5.5 mm and subsequently polished using 320 grit SiC paper and water to remove any surface defects or oxidation. RUS is a nondestructive vibration-based technique used to measure the elastic properties of solid samples [16]. A commercial system (RUS008) was used to determine G before and after heat treatment [16]. In situ RUS measurements were taken using a high-temperature stage employing alumina buffer rods attached to piezoelectric transducers in a sealed chamber. Samples were mounted with the diagonally opposite corners in contact with the piezoelectric transducers to approximate the free boundary conditions. Samples were heated at a rate of 45 °Cmin^{-1} to 400 °C, followed by a 24 h heat treatment at 400 °C in flowing argon gas. Resonance spectra were collected every 15 seconds for the first 2 h of the 24 h test, then every 5 minutes thereafter. The excitation frequencies were between 170 to 194 kHz. A complete fit using an isotropic model was hindered by texturing in the samples. Since the first peak was almost entirely c44 dependent, the shear modulus could be determined by converting the frequency of the peak positions into c44 using Equation 1, where F was the frequency of the first peak and A was a multiplication factor determined from the fit of the RT RUS scan after the 24 h aging and cooling.

$$c44 = A * (F^2) \quad (1)$$

Conventional uniaxial tensile tests were performed using an MTS® servo-hydraulic testing machine equipped with an MTS® Flex Test SE controller in a RT air environment. The displacement rate was 0.025 mmsec^{-1}, which corresponded to a strain rate of approximately 0.001 s^{-1}. An alumina-arm extensometer with a 12 mm gauge length was spring-loaded to the side of the gage section to measure strain during tensile testing. 0.2% yield strength, ultimate tensile stress, and elongation-to-failure were calculated according to ASTM standard E8-E8M-13a, sections 7.7.1, 7.10, and 7.11.5, respectively, and 0.2% yield strength and

ultimate tensile strength values were reported according to section 7.13.1. Two samples were tested per alloy and condition to evaluate the data reproducibility.

Results

Microstructure

The XRD profiles revealed that the ω and α phases precipitated within the TC and TCF microstructures, while only the α phase precipitated within the TCA and TCFA microstructures during the exposures, see Figure 1 for the experimental profiles. These phases precipitated during the first 0.5 h.

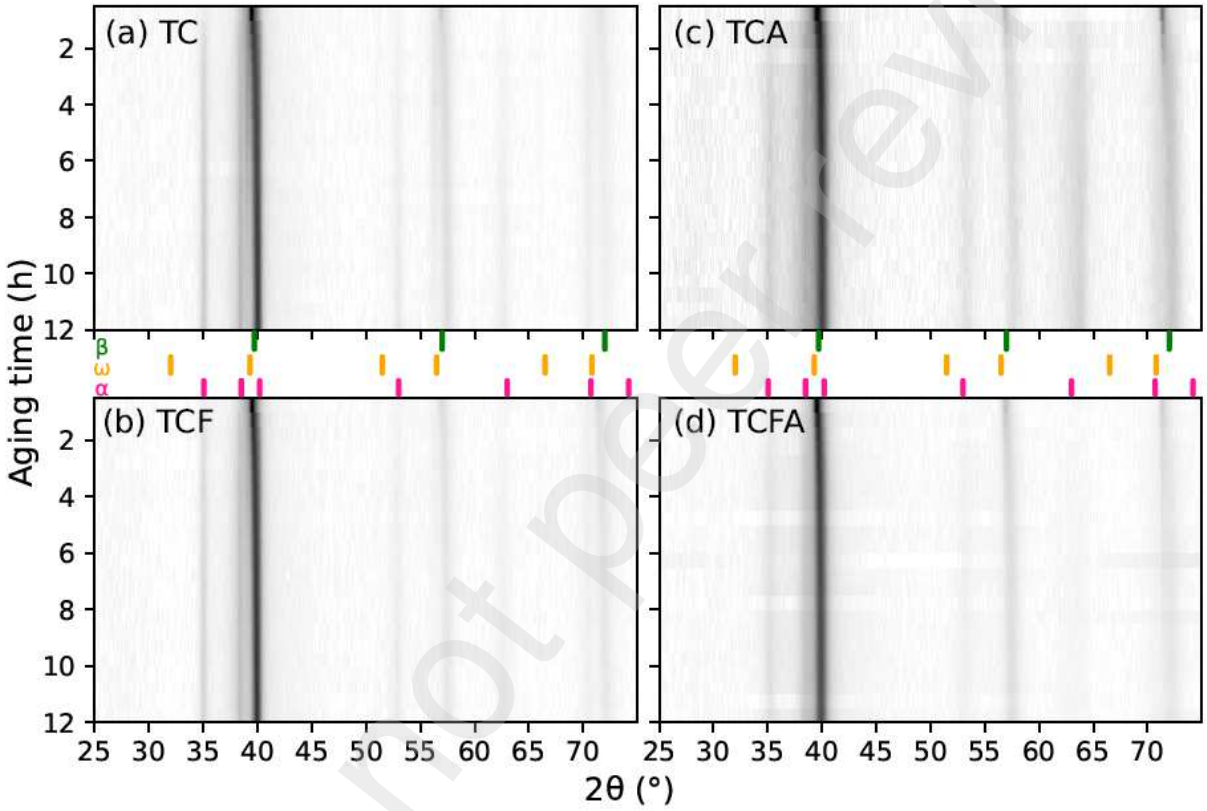

Figure 1. The HTXRD experimental data for (a) TC, (b) TCF, (c) TCA, and (d) TCFA, where a darker value indicates a higher intensity

The α precipitates in TCA and TCFA, see Figures 2(a,b), respectively, exhibited a darker contrast in the lighter β matrix, and they appeared to be randomly distributed throughout the β grains and along the β grain boundaries. During the phase transformations, Cr diffused from the α-phase precipitates into the β matrix, thus the β phase appears brighter in the BSE SEM images [17].

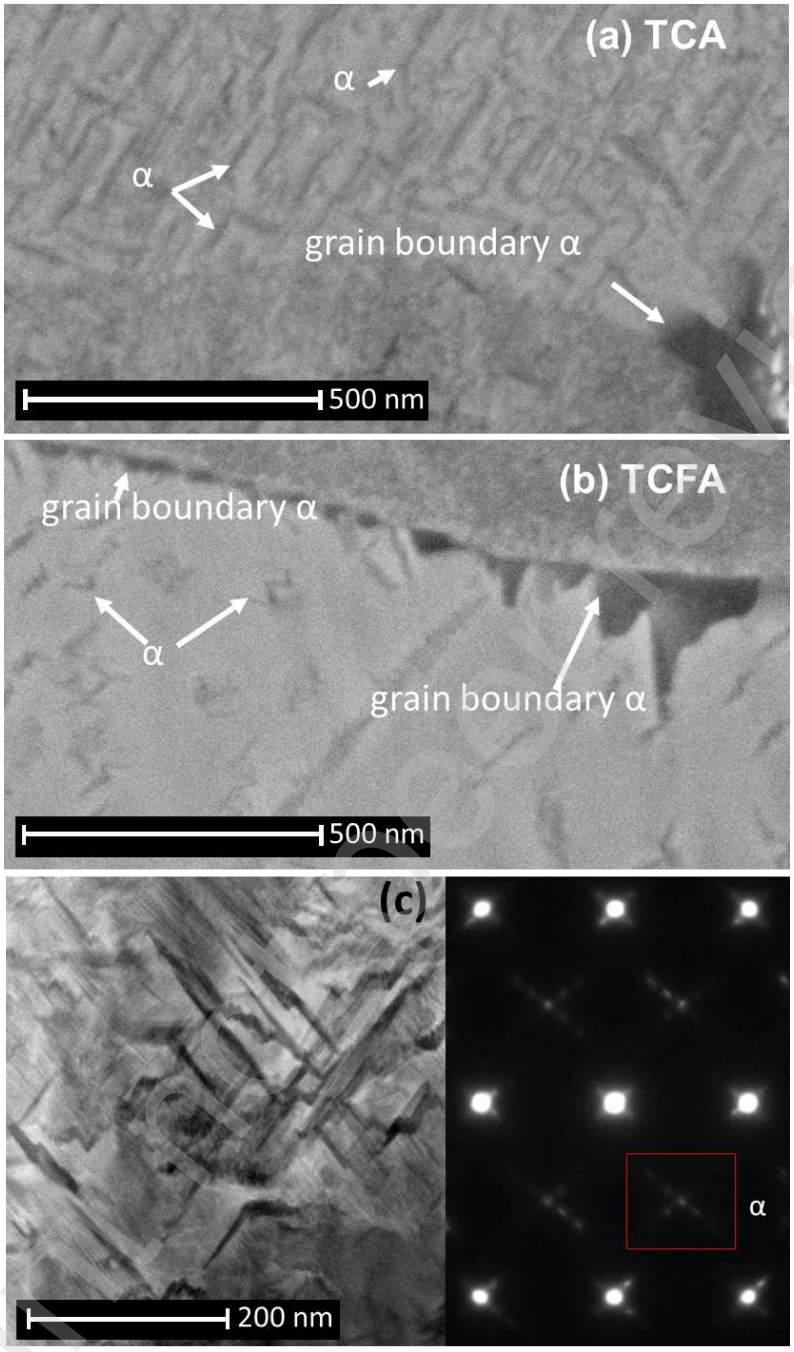

Figure 2. BSE photomicrographs of (a) TCA and (b) TCFA aged for 0.75 h, showing darker precipitates in a lighter β-phase matrix. (c) STEM TCFA image along with the associated selected area diffraction pattern. confirming the lenticular precipitates were α phase.

The grain boundary α phase exhibited an equiaxed morphology instead of a lamellar morphology consistent with that reported in the literature [1,18–20]. The small lenticular precipitates visible within the β grains were consistent with the intergranular α phase [3,4,19–21] and these formed either in small clusters or stacked in lines. The lenticular precipitates in TCFA after 12 h of aging were confirmed to be α-phase through HAADF STEM and SAD imaging, see Figure 2(c).

In TC and TCF, less than 50 nm long cuboidal or ellipsoidal precipitates were observed as darker precipitates in the lighter β-phase matrix, see Figure 3(c,d). These precipitates were consistent with the ω-phase precipitates reported by Bartha et al., [22], see Figure 3(a) and (b). The TC ω-phase precipitates were smaller and greater in number than those in TCF. The lack of these cuboidal or ellipsoidal precipitates in TCA and TCFA (both of which exhibited the two-phase β+α microstructure) also supports that they were the ω phase. If they were α-phase precipitates, similar features would be visible in the TCA and TCFA BSE SEM photomicrographs.

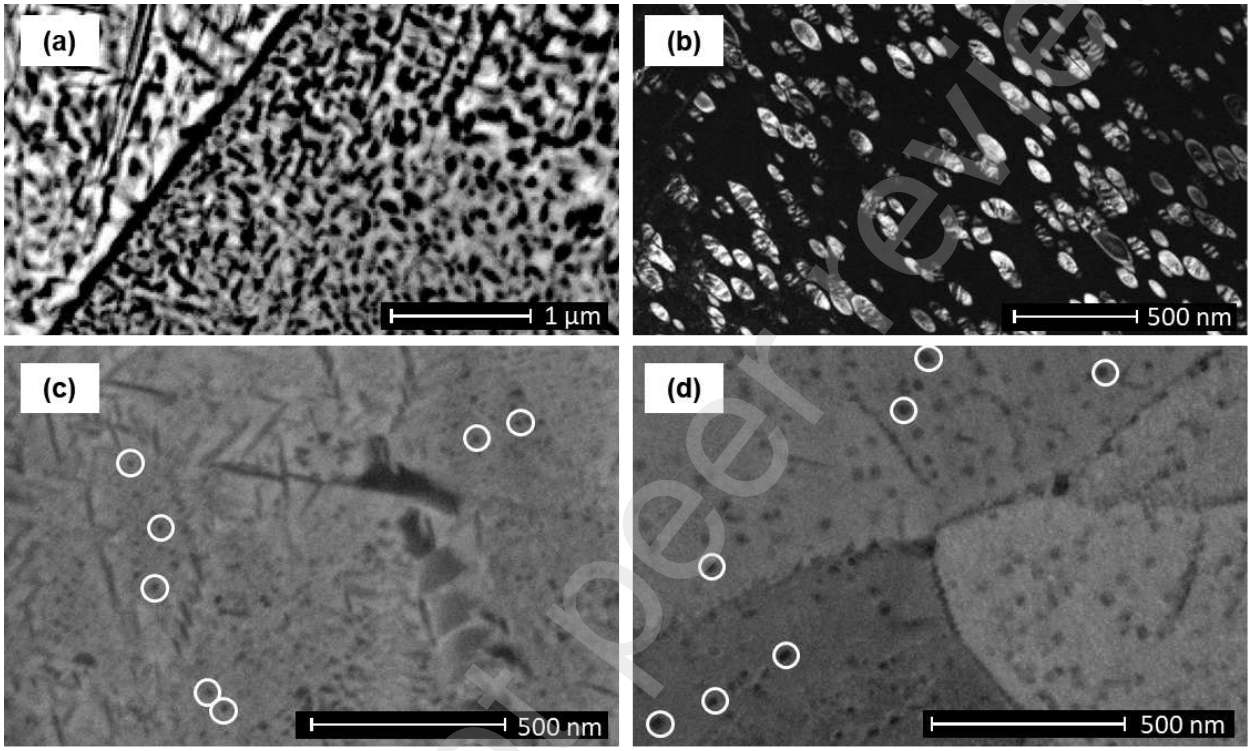

Figure 3. (a) BSE-SEM photomicrograph of a β+ω+α microstructure in Ti-15Mo and (b) corresponding dark-field TEM image using a diffraction spot from one variant of the ω phase from the same microstructure. (a) and (b) are reproduced from Bartha et al. [22]. BSE-SEM photomicrographs of (c) TC and (d) TCF exhibiting several precipitates consistent with the ω phase circled in white.

The Rietveld deconvolutions of the TC and TCF are shown in Figure 4(a,b). To increase the accuracy of the TCF refinement, the ω-phase profiles were removed from the TCF profile analysis for the scans from 8-12 h. For these profiles, the ω-phase peaks were not clearly present, and the analysis used the ω-phase profile as a smoothing function to reduce the error between the calculated and experimental profiles, which produced unrealistic phase profiles and volume fractions for the β, α, and ω phases. Thereafter, the ω-phase was removed from the analysis of TCF for those profiles. Both the broad phase peaks and the overlapping peaks led to some variation in the volume fraction measurements, particularly in TCA, where the broad experimental phase peaks were difficult to refine.

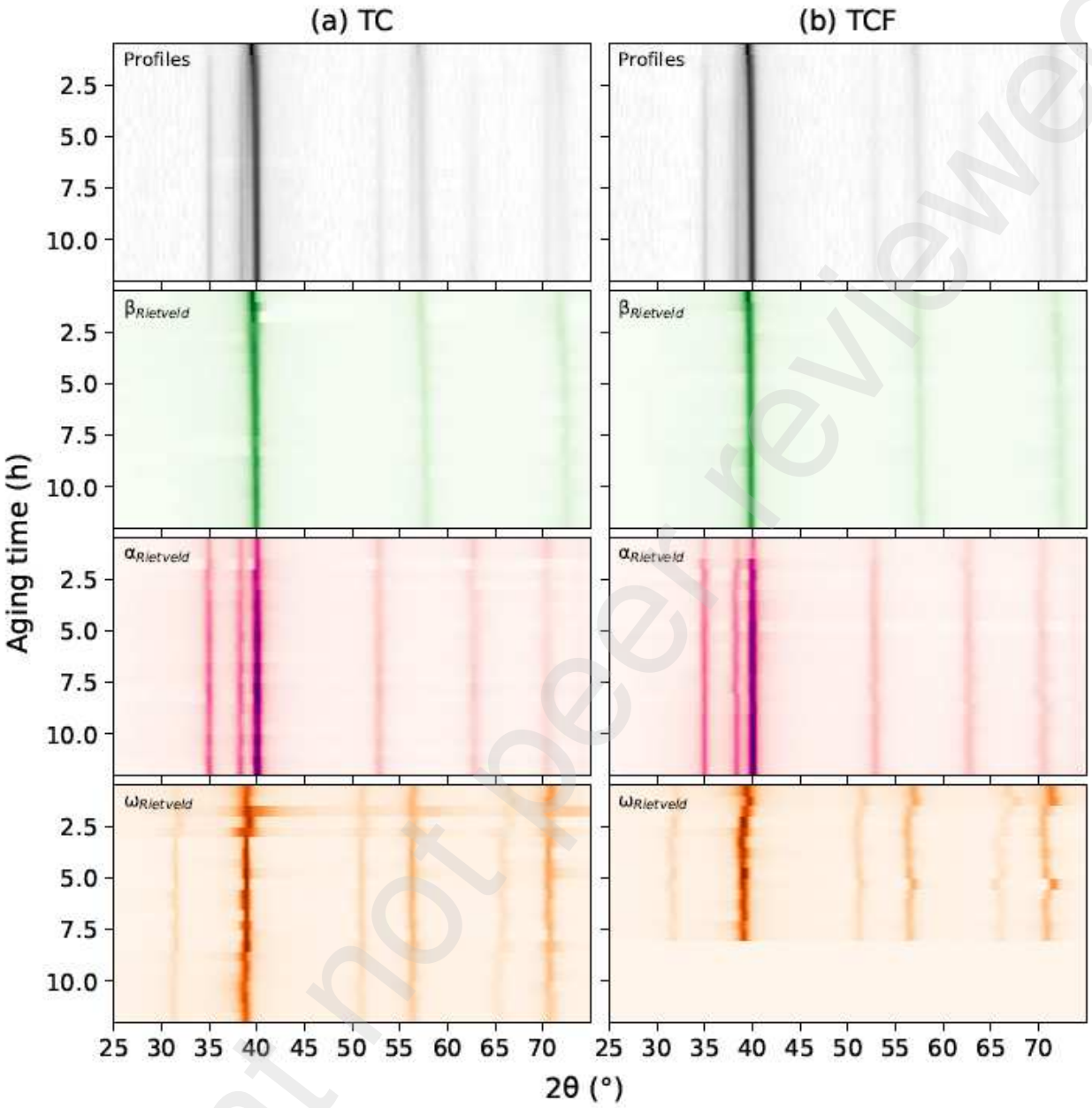

Figure 4. Rietveld deconvolutions of the 400 °C XRD results for (a) TC and (b) TCF.

The Rietveld-calculated β-, α-, and ω-phase volume fractions in each alloy were plotted as a function of aging time, see in Figure 5. Throughout the 12 h aging, the β-phase volume fraction decreased and the α-phase volume fraction increased for each alloy. TC and TCF exhibited the highest ω-phase volume fraction after 0.5 h; the ω-phase volume fractions then decreased with increased aging time. The 0% ω-phase volume fraction in TCF indicates when the ω phase was removed from the deconvolutions.

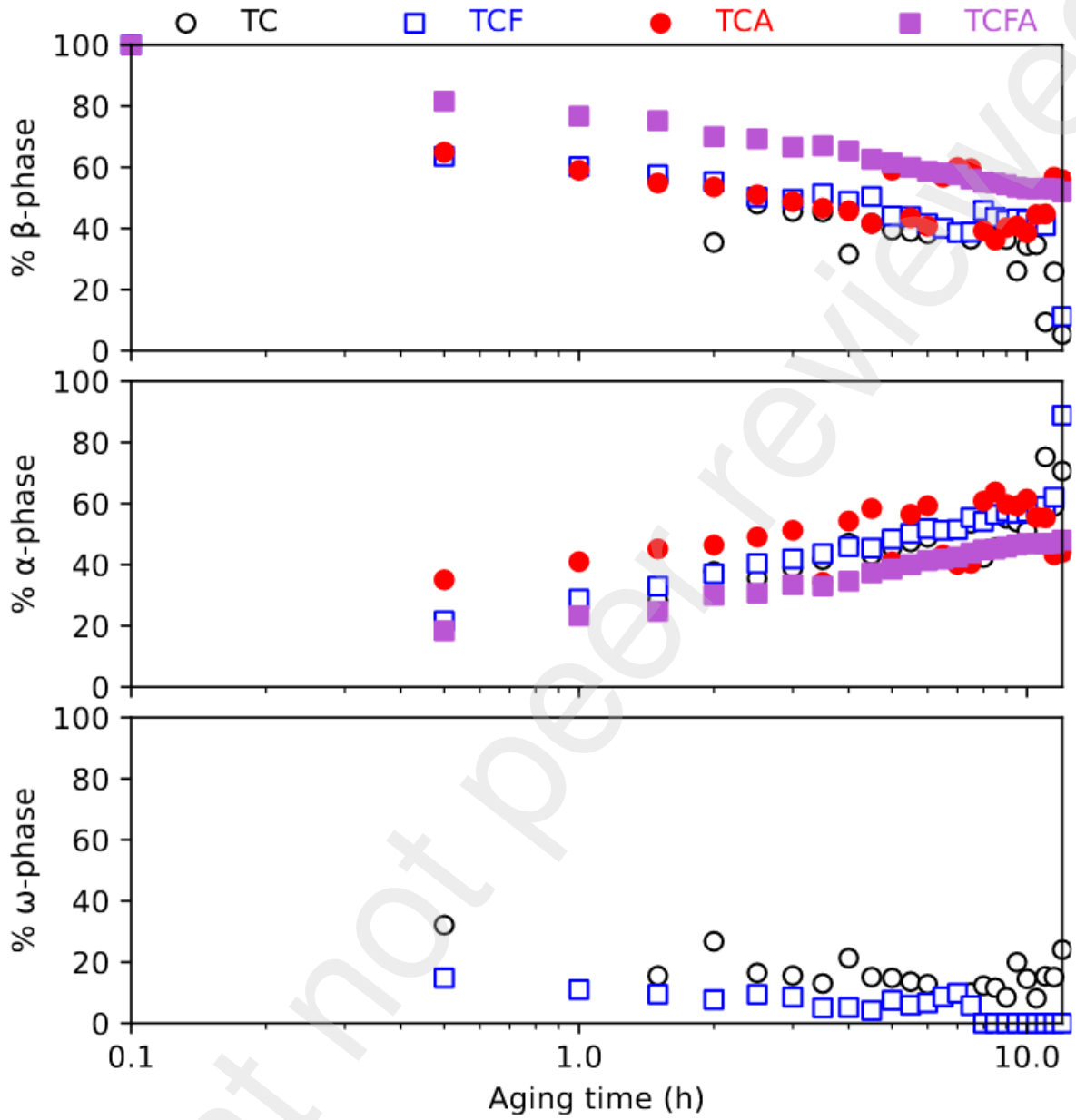

Figure 5. The Rietveld-calculated volume fractions of the (top) β phase, (middle) α phase, and (bottom) ω phase for TC, TCF, TCA, and TCFA as a function of aging time at 400 °C.

The Fe addition in TCF appeared to reduce the ω-phase volume fraction compared to TC. The Fe addition in TCFA appeared to reduce the α-phase volume fraction compared to TCA. The Fe addition did not appear to affect the α-phase volume fraction in TCF compared to TC, as both TC and TCF exhibited similar α-phase volume fractions. The Al addition appeared to promote the β-to-α transformation in TCA, which exhibited the highest α-phase volume fractions of all the alloys.

To verify the Rietveld analysis trends, a second volume fraction analysis, using the BSE-SEM images, was performed. Contrast differences between the β phase and the precipitated phases in the BSE SEM images taken after 0.75, 1.5, 3, and 6 h of aging were exploited, where pixels darker than a set threshold were used to calculate the precipitate volume fractions. This volume fraction analysis could not isolate the ω from the

α phase, due to their similarly dark contrast. Therefore, they were combined in the precipitate volume fraction measurements for TC and TCF. Figure 6 compares the threshold analysis volume fractions to the Rietveld analysis precipitate volume fractions. Although the threshold analysis tended to result in a lower precipitate volume fraction than the Rietveld analysis, they both confirmed that the precipitate volume fraction increased with increased aging time.

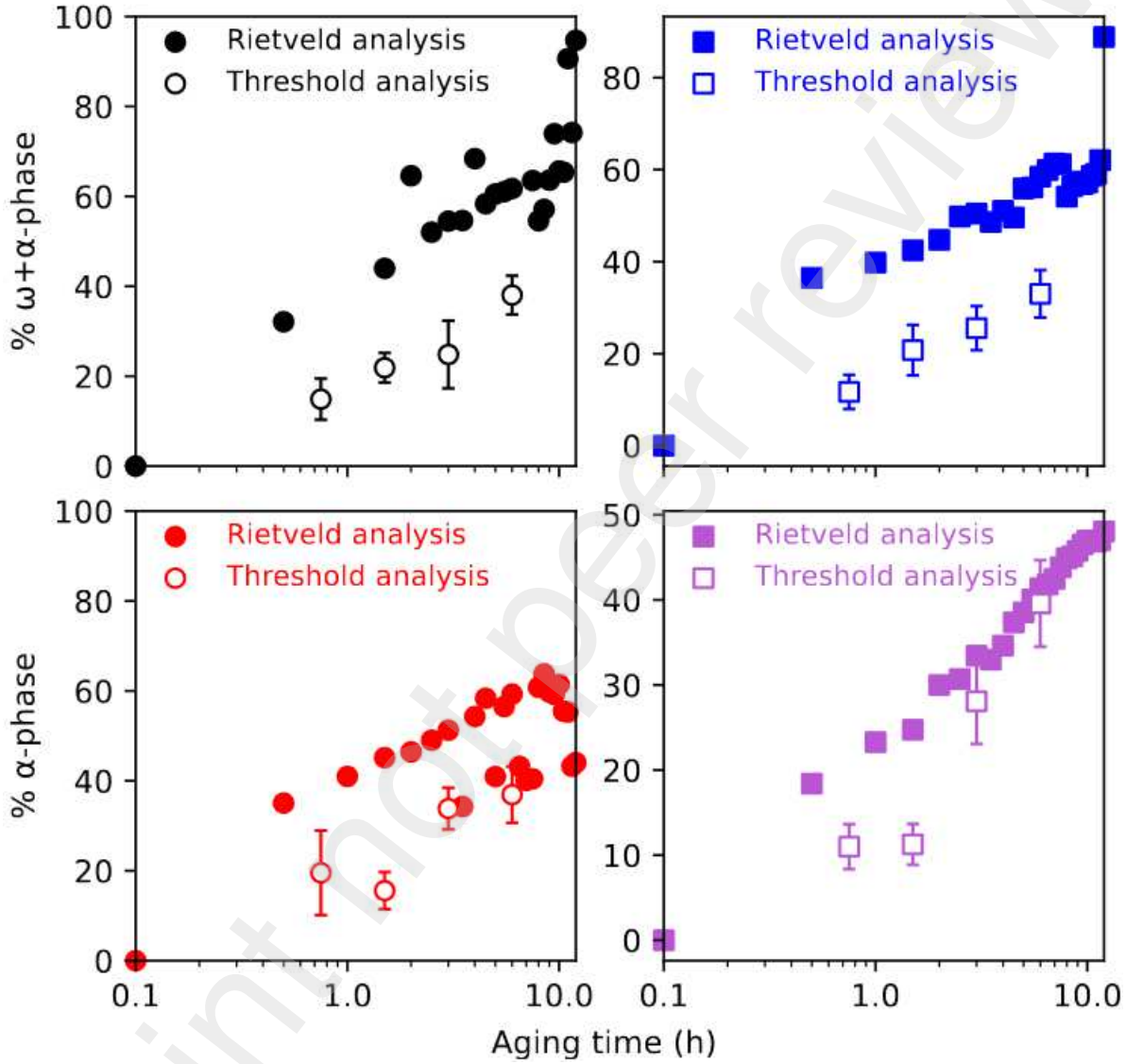

Figure 6. The SEM-based threshold analysis precipitate volume fraction results compared to the XRD-based Rietveld analysis precipitate volume fraction results for (a) TC, (b) TCF, (c) TCA, and (d) TCFA. The Rietveld analysis for TC and TCF included summing the α- and ω-phase volume fractions.

Mechanical properties

The alloys were tested before heat treatment to determine their shear modulus (G), 0.2% yield strength (σ_y), ultimate tensile strength (UTS), and hardness properties in the β-homogenized condition. These values, which are included as the "β" aging time in Figure 7, were used as baseline values to indicate how the aging process changed each property. An explanation of the effects Fe and Al had on the β-homogenized properties can be found in Ballor et al. [11] and Ballor [23]. The Vickers hardness and the tensile properties

of each alloy were measured after 0.75, 1.5, 3, 6, and 12 h of aging, see Figure 7. TC exhibited an increase in hardness after 0.75 h, followed by a subsequent decrease from 1.5 to 6 h, and an increase to its maximum hardness at 12 h. TCF followed a similar evolution, increasing in hardness from 0 to 0.75 h, decreasing to 1.5 h, then increasing for the remainder of the aging. TCA and TCFA exhibited increased hardness with increased aging time. The UTS and σ_y followed similar trends as the hardness, see Figure 8. No further significant increase in Hv was measured for up to 300+ h of 400 °C aging for TC, TCF, TCA, or TCFA [24].

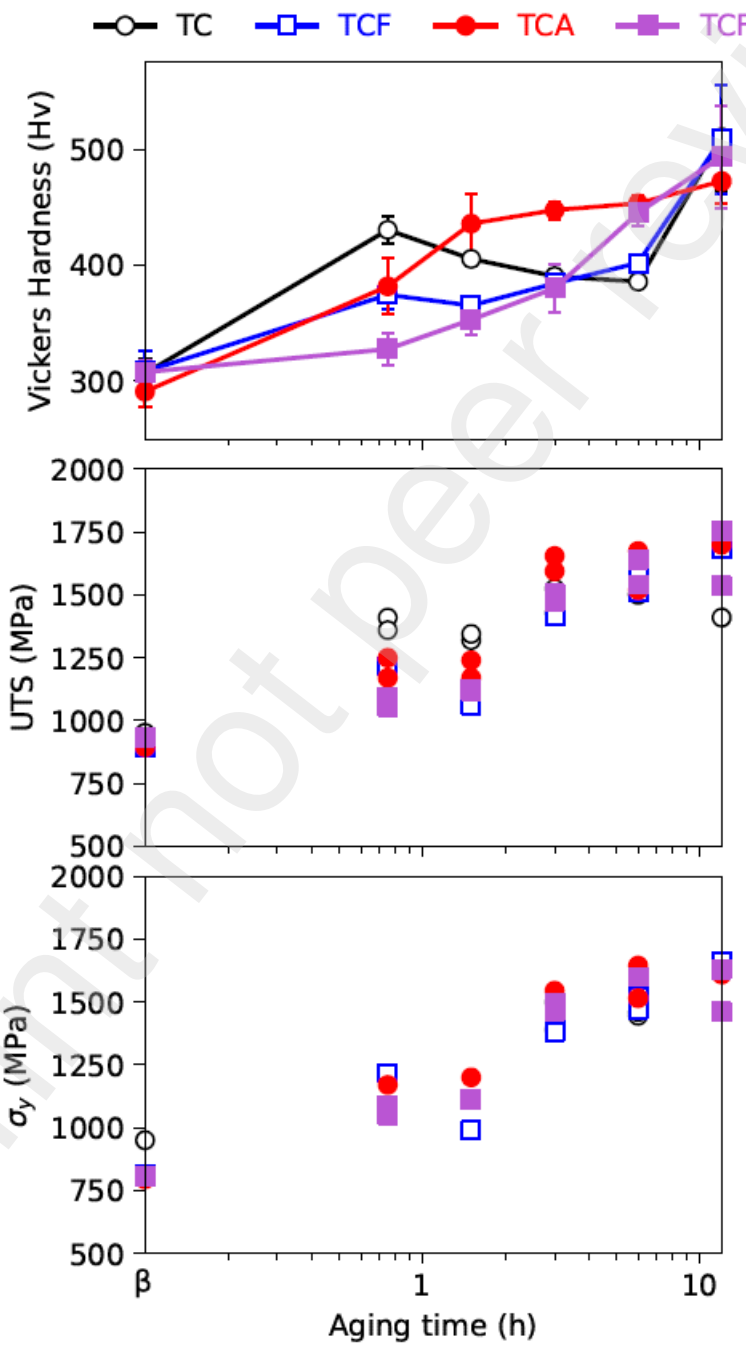

Figure 7. Vickers hardness, UTS, and σ_y as a function of 400 °C aging time for TC, TCF, TCA, and TCFA. No σ_y data points are presented for TC after 0.75 and 1.5 h aging, indicating brittle failure where the 0.2% yield stress could not be calculated according to ASTM E8-E8M-13a.

The ω-containing microstructures (TC and TCF) did not exhibit significantly higher σ_y or UTS values than the ω-free microstructures (TCA and TCFA), see Figure 8. TC exhibited higher UTS values than the other three alloys after 0.75 and 1.5 h. TC exhibited similar UTS and σ_y values for all other aging times. The hardness evolution of TC suggests that both σ_y and UTS should be highest for this alloy after 0.75 h of aging.

The RT G values for TCF, TCA, and TCFA were 33 GPa, 30 GPa, and 33 GPa, respectively, as measured from one sample per alloy. For TC, two samples were measured, and the G values were 37 GPa and 40 GPa. The higher G values exhibited by TC agreed with a higher average bond order between Ti and Cr (2.779) than Ti and Fe (2.651) or Ti and Al (2.426) [25]. Since bond order and bond strength are analogous, a higher average Bo should result in higher G values [25,26].

As the sample temperature increased to 400 °C, the G values of TC, TCF, and TCFA decreased to 34 GPa, 31.5 GPa, and 32 GPa, respectively, and the TCA G value increased to 32 GPa. The decrease in G for TC, TCF, and TCFA can be explained by the softening of the lattice. Because TCA exhibited an increase in G, phase transformations were assumed to have occurred during the 400 °C aging. If transformations occurred during heating in TCA, it is possible that they occurred in the other alloys as well. After reaching 400 °C, both of the three-phase (β+α+ω) TC and TCF alloys exhibited a higher increase in G during the 24 h 400 °C aging than the two-phase (β+α) TCA and TCFA alloys, see Figure 8. With the precipitation of the ω phase during the first 0.5 h at 400 °C, TC exhibited an increase in G of 9 GPa (or 26%) and TCF exhibited an increase in G of 2.5 GPa (or 8%).

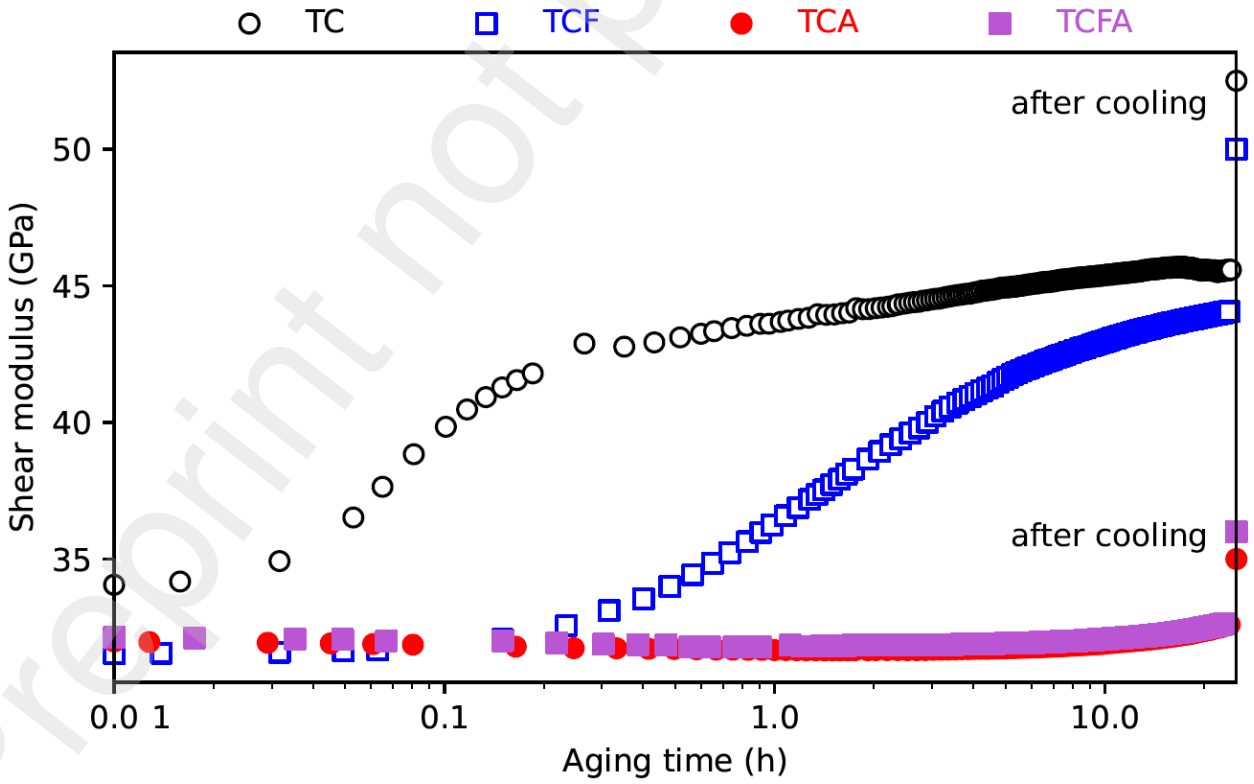

Figure 8. The shear modulus (G) of each alloy at 400 °C measured using RUS as a function of aging time. The 'after cooling' data indicated the data taken after the samples were cooled to RT.

After the 24 h aging, the samples were cooled to RT and the measured G values were 52.5 GPa, 50 GPa, 35 GPa, and 36 GPa for TC, TCF, TCA, and TCFA, respectively. TCF exhibited the largest relative increase in G of 51%, followed by TC, which experienced an increase of 42%, while TCA and TCFA exhibited increases of 17% and 9%, respectively.

Discussion

Composition-microstructure relationship

The addition of the α-phase stabilizer Al into the Ti-Cr alloy system favored the β-to-α transformation more than the β-to-ω transformation. Thus, the ω phase was not formed in TCA or TCFA during the 400 °C aging. However, even though Al promoted the β-to-α transformation over the β-to-ω transformation, the Al-containing TCFA exhibited a lower α-phase volume fraction than the Al-free TC and TCF. Fe is a strong β-phase stabilizer [27], and the β-phase stabilizing effect of Fe resulted in a reduced α-phase volume fraction in TCFA. This effect could have been enhanced by the difference in the Fe and Al diffusion speed at 400 °C. The diffusion coefficients or diffusivities (D) for Cr, Fe, and Al at temperatures between 900 °C and 1350 °C were taken from diffusion data of Ti-18Cr [28], Ti-1Fe alloy [29], and Ti-2.1Al [30], see Figure 9. Extrapolating the trends of D from the 900 °C and 1350 °C temperature range to 400 °C, D was calculated to be 2.98×10^{-16} m^2s^{-1} for Cr, 1.49×10^{-17} m^2s^{-1} for Fe, and 2.48×10^{-19} m^2s^{-1} for Al at 400 °C. The D for Al is 100x lower than the D of Fe, thus Al should diffuse significantly slower than Fe during the β-to-α transformations. In TCFA, Fe would diffuse into the β-phase faster than Al could diffuse to the α phase in TCFA, and the strong β-stabilizing effect of Fe could limit the precipitation and growth of the α phase in TCFA compared to the Fe-free β matrix of TCA. Fe could also prevent the longer-range diffusion needed for α-phase formation [31], which would limit the α-phase volume fraction of TCFA compared to TCA.

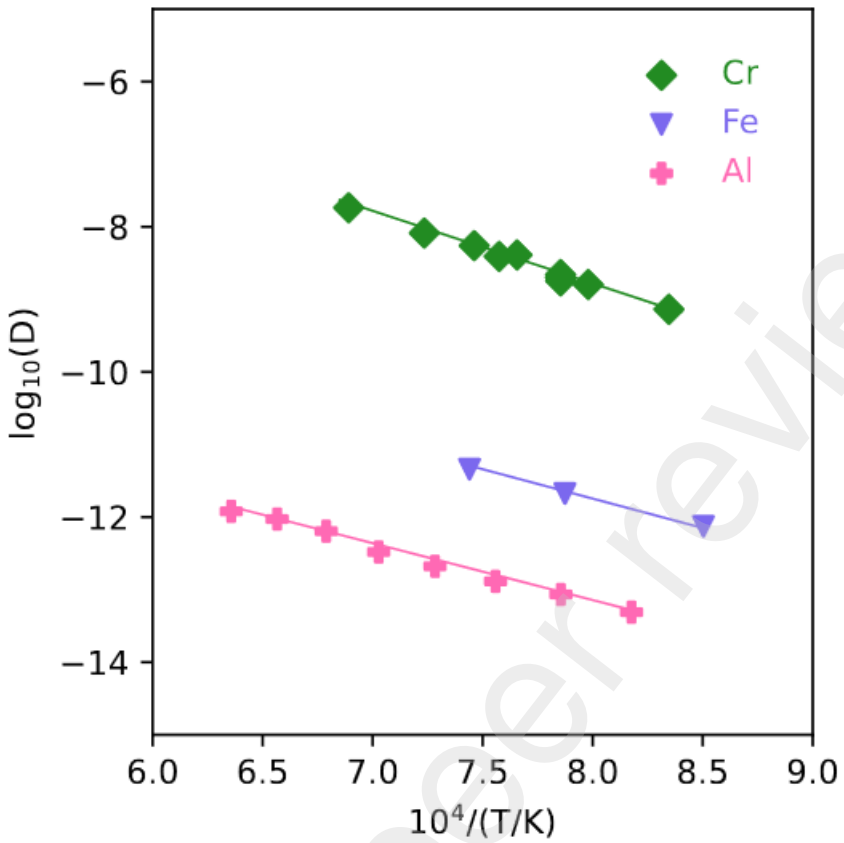

Figure 9. Diffusion data used to calculate the diffusion coefficients (D) for Cr, Fe, and Al in Ti at 400 °C. Data from [28], [29], and [30] were for Cr, Fe, and Al, respectively.

In TCF, the Fe addition could have limited the ω-phase volume fraction in a similar way. The β-to-ω transformation is diffusion controlled [1], where all alloying elements diffuse from the ω phase into the surrounding β matrix, and Fe diffuses approximately 10x slower than Cr, which would be expected to inhibit the β-to-ω transformation in TCF. The higher β-stability from the Fe addition in TCF could have also reduced the free energy of the β phase compared to the ω phase, thereby preventing the β-to-ω transformation in TCF [32].

The Fe addition did not reduce the α-phase volume fraction in TCF compared to TC. The ω phase could have increased the α-phase volume fraction in TCF compared to TCFA through the ω-assisted α-phase transformation. The ledges and interfacial energy at the ω/β boundary would act as a favorable nucleation site for the α phase [3,33–36]. The lack of β-stabilizers in the ω phase could indirectly promote the formation and growth of the α phase [37,38]. The decrease in the ω-phase volume fraction in both TC and TCF could be due to the ω-assisted α-phase transformation, as there is evidence that the α phase consumes the ω phase as it grows [2].

Microstructure-property relationship

For the two-phase β+α microstructures of TCA and TCFA, hardness, σ_y, and UTS increased with increased α-phase volume fraction, see Figure 10.

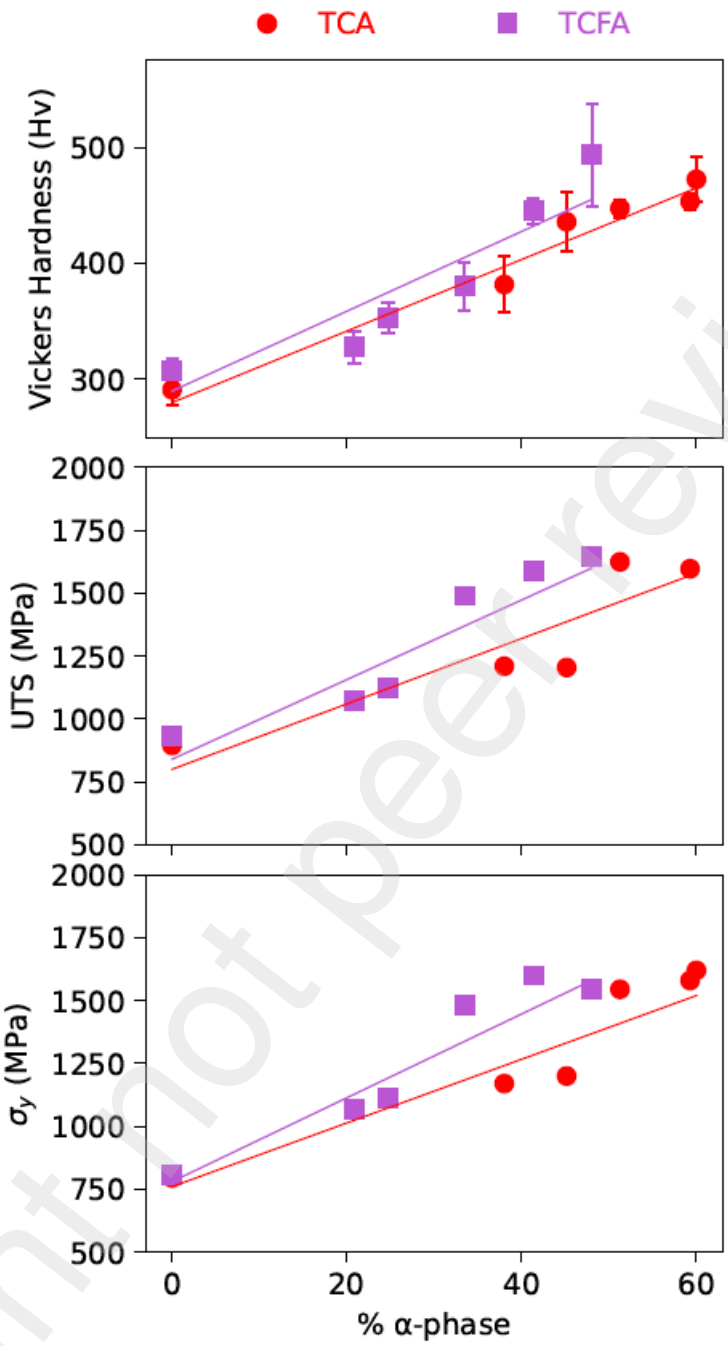

Figure 10. Vickers hardness, σ_y, and UTS as a function of α-phase percentage for TCA and TCFA.

For the three-phase (β+α+ω) microstructures of TC and TCF, the increase in hardness and strength was influenced by both the ω- and α-phase volume fractions. The initial increase in hardness and strength was attributed to the ω-phase volume fraction, and the subsequent decrease in hardness was likewise attributed to the decrease in ω-phase volume fraction in both TC and TCF, even though the α-phase volume fraction was increasing. Although the ω-phase volume fraction continued to decrease with increased aging time, both TC and TCF exhibited an increase in hardness and strength at longer aging times, suggesting that the α phase became the dominant hardening and strengthening phase. This did not occur for a certain volume fraction of α or ω phase. Instead, when the ω/α phase volume fraction ratio fell below 0.25, the hardness

and strength of TC and TCF increased with increased α-phase volume fraction even as the ω-phase volume fraction decreased, see Figure 11. This evolution is less clear in TC due to the brittle failure of the TC samples after 0.75, 1.5, and 12 h aging (indicated with red circles in Figure 11), which prevented the calculation of σ_y for those aging times. The brittle fracture likely prevented higher strengths from being exhibited for those aging times.

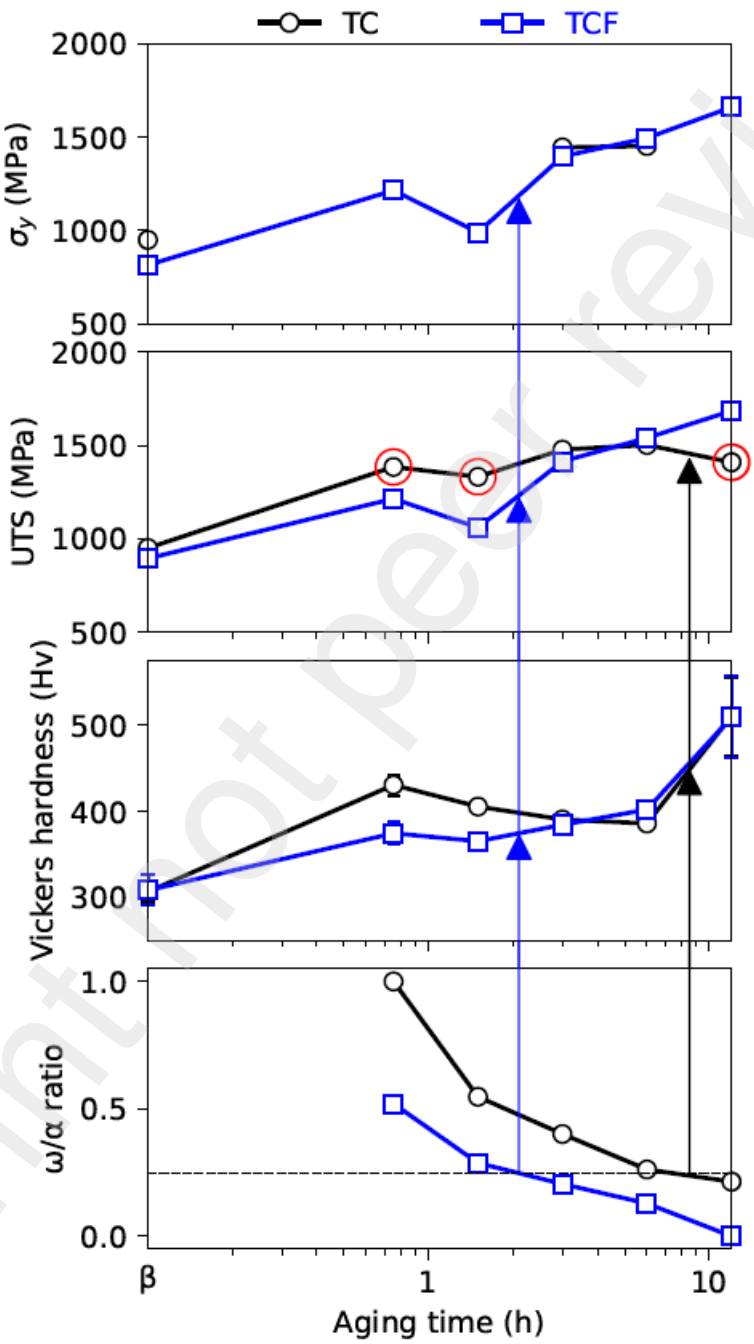

Figure 11. The Vickers hardness and ω/α volume fraction ratio evolutions with increased aging time for TC and TCF. The arrows highlight the increased hardness when the ω/α ratios fell below 0.25. The data

circled in red for TC were for samples which experienced brittle failure and therefore proper s_y was not calculated.

The G values for each alloy were checked to see if they agreed with the rule-of-mixtures (ROM) for multi-phase materials. The ROM for a two-phase material was used to calculate the predicted G values for TCA and TCFA, with the upper bound for the ROM calculated using Equation 2 and the lower bound for the ROM calculated using Equation 3. Because the α and ω phases exhibit different G values along different crystallographic directions, the upper and lower bounds for the ROM were calculated using maximum and minimum G values. For TCA and TCFA, the ω-phase volume fractions were set to zero.

$$G_{max} = G_\beta v_\beta + G_\alpha v_\alpha + G_\omega v_\omega \quad (2)$$

$$G_{min} = \left(\frac{v_\beta}{G_\beta} + \frac{v_\alpha}{G_\alpha} + \frac{v_\omega}{G_\omega}\right)^{-1} \quad (3)$$

Table 2 lists the values used in the ROM. The RUS-measured G values, once 400 °C was reached, were used for G_β of each alloy. It was assumed that these G values were of the β phase of each alloy at 400 °C. The ω-phase G values at 400 °C are not known, so the measured RT values were used. The RUS-measured G values for all alloys fell within the range of values predicted by the ROM, see Figure 12.

Table 2. The values used in the ROM G calculations.

Alloy	G_β (GPa)	G_α <0001>(GPa) [39,40]	G_α <11-20>(GPa) [39,40]	G_ω <0001>(GPa) [39]	G_ω <11-20>(GPa) [39]
TC	34	20	35	45	70
TCF	31.5	20	35	45	70
TCA	32	20	35	na	na
TCFA	32	20	35	na	na

na: not available

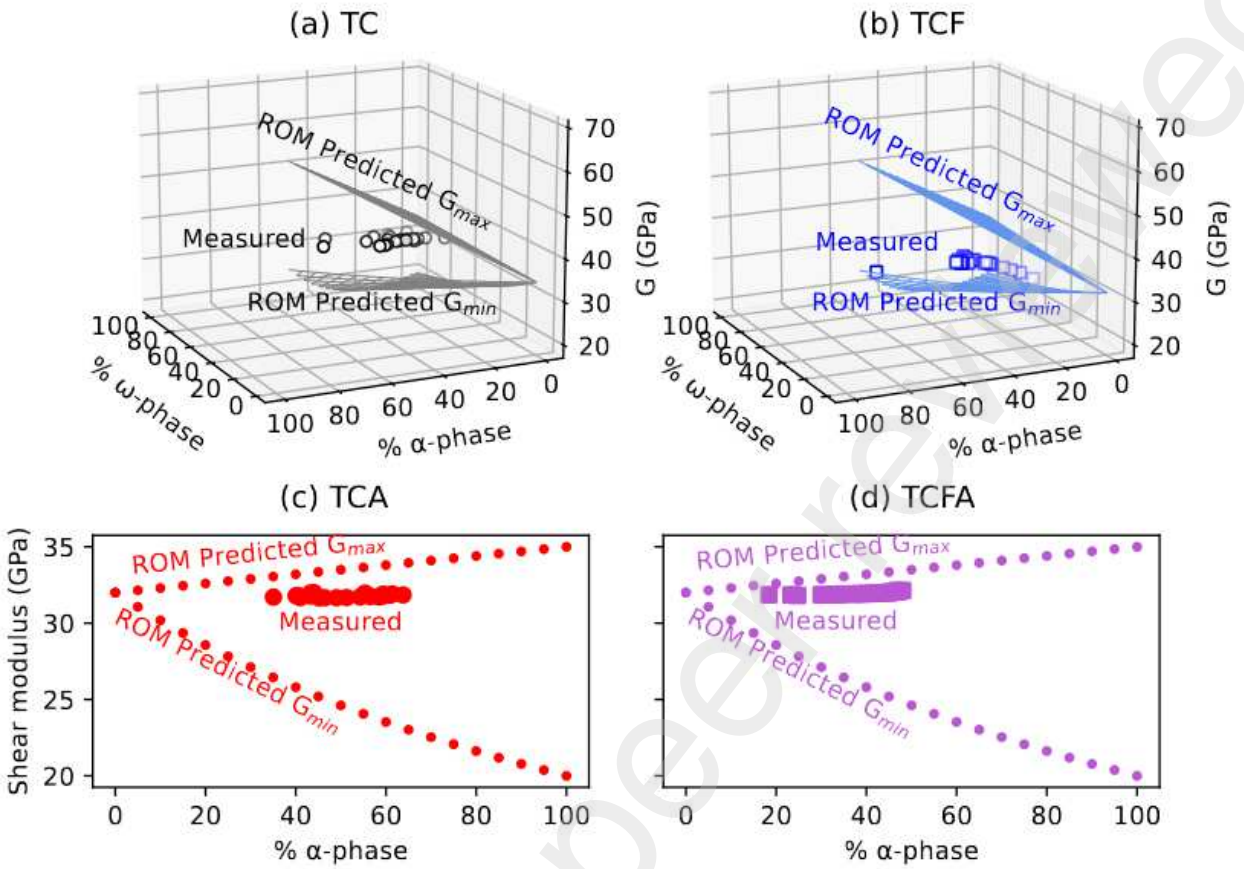

Figure 12. The RUS-measured G values (data points) for (a) TC and (b) TCF compared to the ROM-predicted G values (green and blue contours). The RUS-measured G values for (c) TCA and (d) TCFA compared to the ROM-predicted G values. The G values fell within the range of values predicted by the ROM.

While the values fell within those predicted by the ROM, some questions still remain about the G evolution of TC and TCF with increased aging time. For both TC and TCF, the ω phase volume fractions were highest after 0.5 h aging, and they decreased thereafter with increased aging time. Following the evolution of ω- and α-phase volume fraction, it was expected that the G of TC and TCF should have followed a similar evolution to that of the hardness, σ_y, and UTS values: an initial increase, followed by a decrease, followed by a further increase once enough α-phase formed in the microstructure, see Figure 11. Instead, G increased as the ω-phase volume fraction decreased, see Figure 13. This increase is clearly related to the ω phase, as TCA and TCFA (β+α microstructures) exhibited significantly lower G values, while they also exhibited similar or greater fractions of the α phase, see Figure 13.

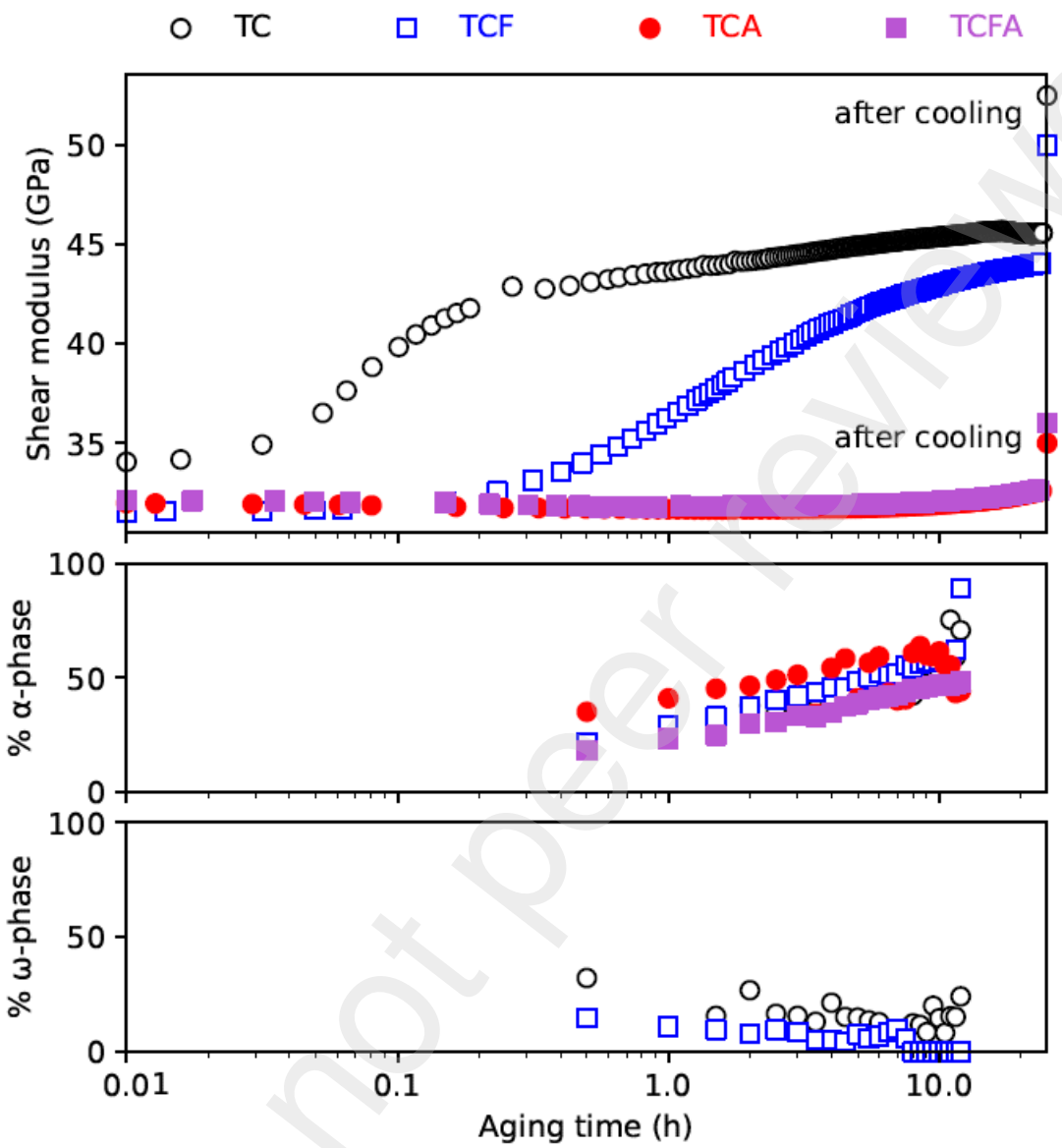

Figure 13. The shear modulus (G) and α- and ω-phase percentages as a function of aging time at 400 °C for each alloy.

The increase in G in TC and TCF could be purely due to the higher G of the ω phase compared to the β or α phases, see Table 2. ω-phase precipitates are known to change morphology and coherency as they grow [42,43], and this coherency has been observed to affect elastic moduli in other systems [44]. In addition, ω precipitates have been shown to elastically interact, affecting their morphology [43]. These elastic interactions could also have an effect on G even as the overall volume fraction of the ω phase decreases. Also, during the β-to-ω and β-to-α transformations the β-stabilizers Cr and Fe diffuse into the β-matrix, affecting the β-phase lattice parameters, which would influence the inherent strain in the lattice [17].

The ω phase could also affect G in TC and TCF by assisting in α -phase precipitation. The ω-assisted α phase was not confirmed in TC and TCF, but in Figure 3(c,d) some lenticular α-phase precipitates appear near precipitates consistent with ω-phase morphology, suggesting that the ω-assisted α phase could have formed in these alloys.

The ω-assisted α phase has been shown to have a significantly deviated habit plane compared to non-ω-assisted α phase [41]. As the α-phase G is anisotropic, the deviated habit plane of the ω-assisted α phase could affect G differently in TC and TCF compared to TCA and TCFA.

Further investigation into how the ω phase causes such a significant increase in G even as the ω-phase volume fraction decreases would be valuable.

Conclusions

Fe and Al were added to a base Ti-11Cr(at.%) alloy to determine their effect on microstructure evolution during 400 °C aging. Ti-11Cr(at.%) underwent the β-to-ω and β-to-α transformations. The Fe addition to Ti-11Cr(at.%) reduced the volume fraction of the ω phase. No ω phase formed when Al was present. When added to Ti-11Cr-5.3Al(at.%), Fe reduced the α-phase volume fraction.

The relationship between ω- and α-phase ratio and mechanical properties has been shown for the first time. The hardness and strength values of TC and TCF increased with increasing ω-phase volume fraction when the ω/α ratio was greater than 0.25. When the ω/α phase ratio was less than 0.25, the hardness and strength increased with increasing α-phase volume fraction. Precipitating the ω phase resulted in an increase in G of ~140% compared to an increase of ~102% in the ω-free microstructures.

Acknowledgments

This material is based in part on work supported by the U.S. Department of Energy, Office of Science, Office of Workforce Development for Teachers and Scientists, Office of Science Graduate Student Research (SCGSR) program. The SCGSR program is administered by the Oak Ridge Institute for Science and Education for the DOE under contract number DE-SC0014664. The authors would like to thank Dr. Bharat Gwalani for his work in obtaining the STEM image shown in Figure 2(c). The funding for the alloy processing, metallographic preparation, and HTXRD was supported by National Science Foundation Division of Material Research (grant No. DMR1607942) through the Metals and Metallic Nanostructures (MMN) program. A portion of the funding for this research was supported by the U.S. Department of Energy, Office of Basic Energy Science through grant No. DE-SC0001525. STM acknowledges support via the Inamori Professorship which supported the in-situ XRD measurements and analysis. The authors acknowledge Dr. Masahiko Ikeda of Kansai University for donating the materials studied and useful insights. A. S. has received funding from the National Science Foundation Award No. 2045122.

Data Availability

The raw and/or processed data required to reproduce these findings cannot be shared at this time as the data also forms part of an ongoing study.

References

[1] G. Lütjering, J.C. Williams, Titanium, 2nd ed., Springer, Berlin, 2007.
[2] J. Ballor, T. Li, F. Prima, C.J. Boehlert, A. Devaraj, A review of the metastable omega phase in beta titanium alloys: the phase transformation mechanisms and its effect on mechanical properties, Int. Mater. Rev. 68 (2022) 26–45. https://doi.org/10.1080/09506608.2022.2036401.
[3] Y. Zheng, R.E.A. Williams, D. Wang, R. Shi, S. Nag, P. Kami, J.M. Sosa, R. Banerjee, Y. Wang, H.L. Fraser, Role of ω phase in the formation of extremely refined intragranular α precipitates in metastable β-titanium alloys, Acta Mater. 103 (2016) 850–858. https://doi.org/10.1016/j.actamat.2015.11.020.

[4] S. Sadeghpour, S.M. Abbasi, M. Morakabati, S. Bruschi, Correlation between alpha phase morphology and tensile properties of a new beta titanium alloy, Mater. Des. 121 (2017) 24–35. https://doi.org/10.1016/j.matdes.2017.02.043.
[5] S. Azimzadeh, H.J. Rack, Phase transformations in Ti-6.8Mo-4.5Fe-1.5Al, Metall. Mater. Trans. A. 29 (1998) 2455–2467. https://doi.org/10.1007/s11661-998-0217-8.
[6] H.-C. Hsu, S.-C. Wu, S.-K. Hsu, C.-T. Li, W.-F. Ho, Effects of chromium addition on structure and mechanical properties of Ti–5Mo alloy, Mater. Des. 1980-2015. 65 (2015) 700–706. https://doi.org/10.1016/j.matdes.2014.09.077.
[7] W.-F. Ho, C.-H. Pan, S.-C. Wu, H.-C. Hsu, Mechanical properties and deformation behavior of Ti–5Cr–xFe alloys, J. Alloys Compd. 472 (2009) 546–550. https://doi.org/10.1016/j.jallcom.2008.05.015.
[8] J.M. Silcock, An X-ray examination of the ω phase in TiV, TiMo and TiCr alloys, Acta Metall. 6 (1958) 481–493.
[9] V. Chandrasekaran, R. Taggart, D.H. Polonis, An electron microscopy study of the aged omega phase in Ti-Cr alloys, Metallography. 11 (1978) 183–198. https://doi.org/10.1016/0026-0800(78)90035-6.
[10] J.L. Murray, Phase diagrams of binary titanium alloys, ASM International, Metals Park, Ohio, 1987.
[11] J. Ballor, M. Ikeda, E.J. Kautz, C.J. Boehlert, A. Devaraj, Composition-Dependent Microstructure-Property Relationships of Fe and Al Modified Ti-12Cr (wt.%), JOM. 71 (2019) 2321–2330. https://doi.org/10.1007/s11837-019-03467-y.
[12] Rigaku, Integrated X-ray Powder Diffraction Software PDXL, Rigaku J. 26 (2010) 23–27.
[13] J.L. Taylor, Duwez, P., Trans Amer Soc Met. 44 (1952).
[14] R.R. Pawar, V.T. Deshpande, Acta Crystallogr Sec. (n.d.).
[15] Ye.S. Chebotareva, S.G. Nuzhdina, Phys Met Met. 36 (1973).
[16] F.F. Balakirev, S.M. Ennaceur, R.J. Migliori, B. Maiorov, A. Migliori, Resonant ultrasound spectroscopy: The essential toolbox, Rev. Sci. Instrum. 90 (2019) 121401. https://doi.org/10.1063/1.5123165.
[17] J. Ballor, J. Poplawsky, A. Devaraj, S. Misture, C.J. Boehlert, The Effect of ω- and α-Phase Precipitation on the β-Phase Lattice Parameters During 400 °C aging in Ti-11Cr(at.%), Microsc. Microanal. 28 (2022) 748–752. https://doi.org/10.1017/S1431927622003440.
[18] S.M. Jagadeesh Babu, P.S. Kataraki, K.S. Narayanaswamy, Phase transformation and microstructure evolution study in various alloy systems: An insight, IOP Conf. Ser. Mater. Sci. Eng. 505 (2019) 012149. https://doi.org/10.1088/1757-899X/505/1/012149.
[19] C. Tan, Y. Fan, Q. Sun, G. Zhang, Improvement of the Crack Propagation Resistance in an α + β Titanium Alloy with a Trimodal Microstructure, Metals. 10 (2020) 1058. https://doi.org/10.3390/met10081058.
[20] T.S. Prithiv, Z. Kloenne, D. Li, R. Shi, Y. Zheng, H.L. Fraser, B. Gault, S. Antonov, Grain boundary segregation and its implications regarding the formation of the grain boundary α phase in the metastable β-Titanium Ti–5Al–5Mo–5V–3Cr alloy, Scr. Mater. 207 (2022) 114320. https://doi.org/10.1016/j.scriptamat.2021.114320.
[21] B. Zhang, Y. Chong, R. Zheng, Y. Bai, R. Gholizadeh, M. Huang, D. Wang, Q. Sun, Y. Wang, N. Tsuji, Enhanced mechanical properties in β-Ti alloy aged from recrystallized ultrafine β grains, Mater. Des. 195 (2020) 109017. https://doi.org/10.1016/j.matdes.2020.109017.
[22] K. Bartha, J. Stráský, A. Veverková, J. Veselý, M. Janeček, Observation of the omega phase particles in Ti15Mo alloy by electron microscopy, Mater. Lett. 309 (2022) 131376. https://doi.org/10.1016/j.matlet.2021.131376.
[23] J. Ballor, The effects of Fe and Al on the composition, processing, microstructure, and property relationships of Ti-11at.%Cr, Michigan State University, 2022. https://doi.org/doi:10.25335/bmw5-zz56.
[24] H.N. Chakravarty, Effect of Alloying Additions of Aluminium and Iron on the Creep Resistance of Ti-12Cr (Wt.%), Michigan State University, 2019.

[25] M. Morinaga, Y. Murata, H. Yukawa, Molecular Orbital Approach to Alloy Design, in: Appl. Comput. Mater. Model., 2007: pp. 255–306.
[26] S.O. Kasap, Principles of Electronic Materials and Devices, 3rd ed., McGraw-Hill, n.d.
[27] P.J. Bania, Beta titanium alloys and their role in the titanium industry, JOM. 46 (1994) 16–19. https://doi.org/10.1007/BF03220742.
[28] A.J. Mortlocks, D.H. Tomlm, The atomic diffusion of chromium in the titanium-chromium system, Philos. Mag. 4 (1959) 628–643. https://doi.org/10.1080/14786435908238259.
[29] H. Nakajima, S. Ohshidat, K. Nonakat, Y. Yoshida, F.E. Fujital, Diffusion of Fe in β Ti-Fe alloys, Scr. Mater. 34 (1996) 949–953.
[30] H. Araki, T. Yamane, Y. Minamino, S. Saji, Y. Hana, S.B. Jung, Anomalous Diffusion of Aluminum in β-Titanium, Metall. Mater. Trans. A. 25 (1994) 874–876.
[31] G.R. Bak, J.W. Won, H.-J. Choe, C.H. Park, Y.-T. Hyun, Effect of iron content on β→α phase transformation behavior of Ti-5Al-xFe (x=1, 2.5, 4) alloys during continuous cooling, J. Mater. Res. Technol. 8 (2019) 2887–2897. https://doi.org/10.1016/j.jmrt.2019.02.020.
[32] J. Min, Y. Guo, J. Niu, J. Cao, Z. Sun, H. Chang, The Characteristic of Fe as a β-Ti Stabilizer in Ti Alloys, Materials. 14 (2021) 7516. https://doi.org/10.3390/ma14247516.
[33] Y. Zheng, R.E.A. Williams, J.M. Sosa, Y. Wang, R. Banerjee, H.L. Fraser, The role of the ω phase on the non-classical precipitation of the α phase in metastable β-titanium alloys, Scr. Mater. 111 (2016) 81–84. https://doi.org/10.1016/j.scriptamat.2015.08.019.
[34] T.W. Duerig, G.T. Terlinde, J.C. Williams, Phase transformations and tensile properties of Ti-10V-2Fe-3AI, Metall. Trans. A. 11 (1980) 1987–1998. https://doi.org/10.1007/BF02655118.
[35] R. Shi, Y. Zheng, R. Banerjee, H.L. Fraser, Y. Wang, ω-Assisted α nucleation in a metastable β titanium alloy, Scr. Mater. 171 (2019) 62–66. https://doi.org/10.1016/j.scriptamat.2019.06.020.
[36] T. Li, D. Kent, G. Sha, H. Liu, S.G. Fries, A.V. Ceguerra, M.S. Dargusch, J.M. Cairney, Nucleation driving force for ω-assisted formation of α and associated ω morphology in β-Ti alloys, Scr. Mater. 155 (2018) 149–154. https://doi.org/10.1016/j.scriptamat.2018.06.039.
[37] F. Prima, P. Vermaut, G. Texier, D. Ansel, T. Gloriant, Evidence of α-nanophase heterogeneous nucleation from ω particles in a β-metastable Ti-based alloy by high-resolution electron microscopy, Scr. Mater. 54 (2006) 645–648. https://doi.org/10.1016/j.scriptamat.2005.10.024.
[38] F. Prima, P. Vermaut, D. Ansel, J. Debuigne, ω Precipitation in a Beta Metastable Titanium Alloy, Resistometric Study, Mater. Trans. JIM. 41 (2000) 1092–1097.
[39] M. Tane, Y. Okuda, Y. Todaka, H. Ogi, A. Nagakubo, Elastic properties of single-crystalline ω phase in titanium, Acta Mater. 61 (2013) 7543–7554. https://doi.org/10.1016/j.actamat.2013.08.036.
[40] U. Argaman, G. Makov, First-principles study of the temperature dependence of the elastic constants of hcp titanium, Comput. Mater. Sci. 184 (2020) 109917. https://doi.org/10.1016/j.commatsci.2020.109917.
[41] Y. Ohmori, H. Natsui, K. Nakai, Crystallographic Analysis of α Phase Formation in a Metastable β Ti Alloy, Mater. Trans. JIM. 39 (1998) 49–56.
[42] M.J. Blackburn, J.C. Williams, Phase Transformations in Ti-Mo and Ti-V Alloys, Trans. Metall. Soc. AIME. 242 (1968) 2461–2469.
[43] F. Prima, P. Vermaut, T. Gloriant, J. Debuigne, D. Ansel, Experimental evidence of elastic interaction between ω nanoparticles embedded in a metastable β titanium alloy, J. Mater. Sci. Lett. 21 (2002) 1935–1937.
[44] C.M. Gilmore, V. Provenzano, Embedded-atom-method study of coherency and elastic moduli of Pd-Cu multilayers, Phys. Rev. B. 42 (1990) 6899–6905. https://doi.org/10.1103/PhysRevB.42.6899.